Journal of Materials Chemistry A

ROYAL SOCIETY OF CHEMISTRY

COMMUNICATION

View Article Online
View Journal | View Issue

Cite this: J. Mater. Chem. A, 2025, 13, 24455

Received 29th May 2025
Accepted 10th July 2025

DOI: 10.1039/d5ta04320d

rsc.li/materials-a

Reconstructing a Gd^{3+}-enriched inner Helmholtz plane with a dynamic electrostatic shielding effect for highly reversible Zn–bromine flow batteries†

Guangyu Zhu,[ab] Yichan Hu,[b] Zhenglin Li,[b] Wei Xiong, *[d] Haibo Hu *[a] and Guojin Liang *[bc]

Zinc–bromine flow batteries (ZBFBs) are promising candidates for large-scale energy storage, with their cycling lifetime determined by the reversibility of the Zn anode. However, dynamic fluctuations in ion concentration within the Inner Helmholtz Plane (IHP) at the Zn anode–electrolyte interface inevitably induce Zn^{2+} ion concentration polarization and tip effects, resulting in dendrite growth and the hydrogen evolution reaction (HER), thus ultimately shortening the battery cycling lifetime. In this work, a Gd^{3+}-enriched IHP is reconstructed by dynamically adsorbing Gd^{3+} cations to maintain a uniform Zn^{2+} ion concentration and stabilize the electric field distribution within the IHP. Specifically, the selective adsorption of Gd^{3+} ions promotes preferential growth of the Zn (101) crystal facet and repels protons, thereby simultaneously suppressing Zn dendrite growth and the HER. Benefiting from the highly stable IHP of the reversible Zn anode, the Zn||Zn symmetric flow battery demonstrates over 10 000 cycles (more than 2000 hours) with an ultra-high cumulative areal capacity of 53 A h cm^{-2}. Meanwhile, the ZBFB with Gd^{3+}-electrolyte achieves over 3300 hours of charge–discharge cycling, showing a 22-fold increase in cycling lifetime compared to the control electrolyte. This study provides new insights into designing highly reversible Zn anodes for flow battery systems with commercial grade cycling life.

1 Introduction

Aqueous Zn–bromine flow batteries (ZBFBs) are distinguished by their intrinsic safety, low cost, and high theoretical energy density,[1–4] positioning them as competitive technologies for large-scale energy storage, particularly in renewable energy integration and grid stabilization.[5–8] However, the unsatisfactory cycle lifetime and low coulombic efficiency (CE) of ZBFBs, associated with challenging issues on the Zn anode side, *i.e.*, dendrite growth and the hydrogen evolution reaction (HER), significantly hinder their commercial deployment.[9–11] Moreover, when adopting larger areal capacities and working currents to achieve higher energy and power density of ZBFBs, these irreversible anode side reactions can be exacerbated, further degrading cycling stability.

The reversibility of the Zn anode is fundamentally determined by the stability of ion concentration and the uniformity of ion distribution within the inner Helmholtz plane (IHP), which acts as the interfacial layer between the Zn anode and the electrolytes.[12,13] Specifically, Zn^{2+} cations inside the IHP are gradually consumed during battery charging, *i.e.*, the Zn plating process, and meanwhile they are dynamically refilled from the bulk electrolyte to maintain the stability of ion concentration, as illustrated in Fig. 1a. However, the disparity between Zn^{2+} consumption and replenishment rates leads to non-uniform ion distribution and localized ion accumulation within the IHP. It further gives rise to a non-uniform electric field to induce concentration polarization and tip effects, which consequently induces Zn dendrite growth.[14] Moreover, the as-formed Zn dendrites, rich in charges, provide abundant active reaction sites for adsorption and reduction of protons (H^+), thus resulting in severe HER. This, in turn, leads to the accumulation of residual hydroxide ions (OH^-), which further react with Zn^{2+} cations to form undesirable inert by-products within the IHP. These insulating byproducts further disrupt the local ionic environment to exacerbate concentration polarization and tip effects.[15,16] The root cause of the uneven IHP is the inherently unstable ion distribution in this region, which becomes particularly pronounced at high currents.

On account of the above-mentioned reasons, stabilizing the IHP has been proven effective in improving Zn anode reversibility, including electrolyte regulation[17–21] and electrode surface

[a]School of Materials Science and Engineering, Anhui University, Hefei 230601, China. E-mail: haibohu@ahu.edu.cn

[b]Faculty of Materials Science and Energy Engineering, Shenzhen University of Advanced Technology, Shenzhen, 518055, China. E-mail: gj.liang@siat.ac.cn

[c]Institute of Technology for Carbon Neutrality, Shenzhen Institute of Advanced Technology, Chinese Academy of Sciences (CAS), Shenzhen, 518055, China

[d]Institute of Technology for Future Industry, School of Science and Technology Instrument Application Engineering, Shenzhen Institute of Information Technology, 518172, China. E-mail: weixiong4-c@my.cityu.edu.hk

† Electronic supplementary information (ESI) available. See DOI: https://doi.org/10.1039/d5ta04320d

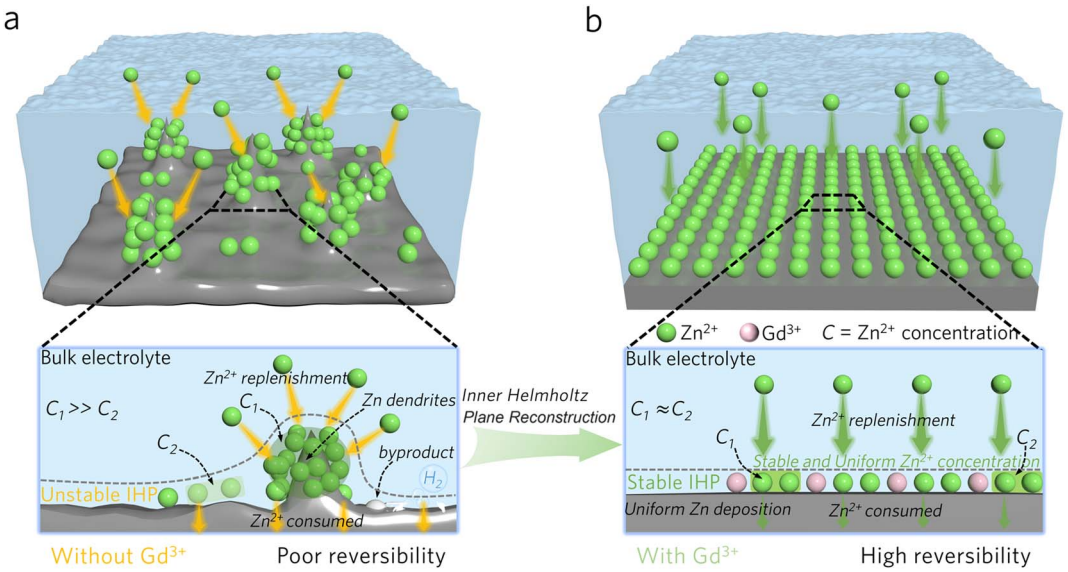

Fig. 1 Relationship between IHP ion concentration stability and Zn anode reversibility. (a) Unstable IHP configuration with non-uniform ion distribution and localized ion accumulation for the irreversible Zn anode with Zn dendrites and the HER, where C_1 and C_2 stand for the Zn^{2+} ion concentrations in two different regions inside the IHP. (b) Stable IHP configuration with uniform ion distribution for a highly reversible Zn anode.

modification,[22–25] both aimed at achieving more uniform ion distribution and stable ion concentration within the IHP. However, it should be noted that the dominant research on IHP regulations of Zn anodes has focused on traditional Zn-ion battery configurations, *i.e.*, the static button and soft pack configurations, with comparatively little attention given to the emerging Zn-based flow batteries. In static configurations, where the electrolyte remains stationary relative to the electrodes, the ion concentration and distribution in the IHP on the electrode during the electrochemical reaction process can reach a relatively stable equilibrium state over time. Consequently, external disturbances to the ion concentration and distribution are minimal. However, in the flow-battery setup, the electrolyte is in a state of continuous flow across the electrodes. Because the continuous influx of the fresh electrolyte with different ionic concentrations constantly replaces the electrolyte near the electrode surface, the ion distribution and concentration within the IHP change more dramatically, thus inducing a severe fluctuation in the number of ions adsorbed or desorbed at the electrode–electrolyte interface involved in the electrochemical reaction. This phenomenon leads to great challenges in maintaining a stable electrochemical environment within the IHP, *i.e.*, the low efficiency of charge transfer, intensified local reactions, and mechanical stress and chemical changes on the electrode surface. This complex interplay between electrolyte flow, ion behavior in the IHP, and electrode–electrolyte interactions is a key area of study in optimizing the energy efficiency of flow batteries.

Regarding IHP modification, some organic additives have been screened and introduced into the electrolytes within button and soft pack configuration, such as MPS,[17] β-CD,[18] pyridine (Py),[19] imidazole group,[20] and malate,[21] which can adsorb within the IHP to uniformly induce a steric hindrance effect to avoid Zn^{2+} aggregation and dendrite growth. Moreover, creating a water-deficient IHP through the *in situ* formation of a PEDOT:PSS hydrogel-based coating layer has been shown to suppress HER side reactions.[22] However, these IHP modification strategies can impede Zn^{2+} deposition kinetics by virtue of steric hindrance, and the surface coating strategy may not be applicable to the three-dimensional electrodes typically used in flow batteries. On the other hand, effective electrode materials have been developed, including N-doped porous carbon electrodes,[23] Zn@ZnS zincophilic electrodes,[24] and Zn@SiO_2-SA electrodes,[25] which provide additional Zn nucleation sites to achieve uniform ion distribution within the IHP. Even though a uniform deposited Zn morphology can be realized, these modifications on electrodes/current collectors are mainly effective at low areal capacities of the Zn anode in Zn-ion battery systems, *e.g.*, typically below 3 mA h cm^{-2}, and the irreversible reaction still occurs after the modified electrode surface is fully covered by thicker deposited Zn. It might not support the desired higher areal capacities, *e.g.*, generally above 10 mA h cm^{-2}, and thus fails to achieve improved energy flow batteries. Therefore, developing an effective IHP modification strategy, which can stabilize ion concentration and homogenize ion distribution on the dynamically changing electrolyte/electrode interface under the continuous flow of electrolytes, is essential for achieving stable and reversible Zn anode chemistry in ZBFBs, but greatly challenging.

In this study, we present an innovative strategy to reconstruct the IHP of zinc deposition on a 3D carbon felt (CF) electrode, serving as the Zn@CF anode for ZBFBs by introducing rare earth element-based cations, *i.e.*, Gd^{3+} ions, into the electrolyte to achieve improved anode/electrolyte interfacial electrochemical chemical stability. Specifically, the Gd^{3+} ions adsorb within the IHP of Zn@CF forming a Gd^{3+}-enriched IHP

that significantly improves the uniformity and stability of ion concentration within the IHP, thereby minimizing ion concentration polarization and edge effects, as illustrated in Fig. 1b. Additionally, this modified IHP forms a stable, dynamic ion adsorption layer, which functions as an electrostatic shielding layer. This layer is highly adaptable to the three-dimensional electrodes in flow batteries. Moreover, the reconstructed IHP influences the growth behaviors of zinc deposition by modulating crystal facet orientation through electrostatic shielding, leading to a distinct Zn (101) crystal orientation on the 3D Zn@CF electrode. The Gd^{3+}-enriched IHP layer also prevents direct contact between the Zn@CF electrode and H^+ ions, effectively suppressing the HER and related byproducts. Thus, this research provides novel perspectives on establishing a Gd^{3+}-enriched IHP, aiming to improve the reversibility of Zn@CF anodes in Zn-based flow batteries.

2 Results and discussion

2.1 Deposition behaviors of Zn^{2+} ions on 3D carbon felt based on the Gd^{3+}-enriched IHP

The utilization of an additive in the electrolyte for the IHP reconstruction of the Zn@CF electrode is investigated by dissolving 0.3 M gadolinium nitrate ($Gd(NO_3)_3$) in 2 M $ZnBr_2$ as the baseline electrolyte, referred to as the Gd^{3+}–$ZnBr_2$ electrolyte. First, the nucleation overpotentials of Zn||Zn symmetric flow batteries are measured, and the battery with the Gd^{3+}–$ZnBr_2$ electrolyte exhibits a higher nucleation overpotential (−51 mV) compared to the battery using the control pure $ZnBr_2$ electrolyte (−31 mV) (Fig. S1†). Additionally, the collected cyclic voltammetry (CV) curves indicate that Zn nucleation in the Gd^{3+}–$ZnBr_2$ electrolyte ($E_1E_2 = 27$ mV) shows a larger polarized potential compared to the pure $ZnBr_2$ electrolyte ($P_1P_2 = 18$ mV, Fig. 2a). These results indicate that the addition of Gd^{3+} ions causes higher energy for Zn^{2+} reduction on the Zn deposit surface during the early nucleation stage. As shown in Fig. 2b, the Zn deposition process is further investigated using chronoamperometry (CA) to characterize the concentration changes of electroactive species in the vicinity of the electrode surface.[26] In the control electrolyte without Gd^{3+} ions, the response current presents a gradual downward trend throughout the entire test. In contrast, the electrolyte with Gd^{3+} ions features a slight decrease in response current within the first 60 seconds and then stabilizes throughout the CA test. This phenomenon indicates that the Zn deposition process has changed from a chaotic 2D diffusion mode into an ordered 3D diffusion mode by introducing Gd^{3+} ions, as illustrated in the inset of Fig. 2b.[27]

On the other hand, no Gd metal is detected on the carbon felt after the electrodeposition process in the Gd^{3+}–$ZnBr_2$ electrolyte, implying that the Gd^{3+} ions are not electrochemically reduced, as confirmed by X-ray photoelectron spectroscopy (XPS) (Fig. S2†) and X-ray diffraction (XRD) (Fig. S3†).[28] This is correlated with the fact that the reduction potential of Zn^{2+} ions (−0.76 V *vs.* SHE, standard hydrogen electrode) is much higher than that of Gd^{3+} ions (−2.27 V *vs.* SHE). Moreover, the zeta potential of the Zn metal in the Gd^{3+}–$ZnBr_2$ electrolyte is 35.13 mV, which is positive and much higher than the value (2.23 mV) observed for the pure $ZnBr_2$ electrolyte (Fig. 2c and S4†). This indicates the specific adsorption of cationic Gd^{3+} ions inside the IHP of the Zn metal, consistent with previous studies showing that metal cations, such as Y^{3+},[29] Sr^{2+},[30] and Ce^{3+},[31] stably adsorb on Zn metal, forming dynamic electrostatic shielding layers to regulate ion distribution and Zn deposition behavior. The Gd^{3+}–$ZnBr_2$ electrolyte exhibits higher ionic conductivity compared to the pure $ZnBr_2$ electrolyte measured at different temperatures (Fig. S5†). Moreover, the activation energies for Zn deposition in the Gd^{3+}–$ZnBr_2$ electrolyte (27.10 kJ mol^{-1}) are relatively higher compared to those in the pure $ZnBr_2$ electrolyte (23.03 kJ mol^{-1}) (Fig. S6†). This suggests that more energy is required to drive Zn^{2+} transfer at the Zn electrode/electrolyte interface in the Gd^{3+}–$ZnBr_2$ electrolyte,[32] which can be attributed to the preferential adsorption of Gd^{3+} ions onto the Zn electrode as an electrostatic shielding layer.[33,34]

High-resolution transmission electron microscopy (HRTEM) analysis is performed to characterize the texture of the deposited Zn metal. Specifically, one major crystalline facet of the Zn deposits in the Gd^{3+}–$ZnBr_2$ electrolyte shows a lattice spacing of 0.209 nm, which corresponds to the $(101)_{Zn}$ facet of Zn (Fig. 2d). In contrast, in the control pure $ZnBr_2$ electrolyte, the deposited Zn displays more lattice fringes of different facets, such as the $(002)_{Zn}$ facet with a spacing of 0.247 nm and the $(100)_{Zn}$ facet with a spacing of 0.231 nm (Fig. 2e). These results imply a preferential growth orientation of the $(100)_{Zn}$ facet in the Gd^{3+}–$ZnBr_2$ electrolyte. To further verify the preferential facet growth, X-ray diffraction (XRD) analysis is conducted on the deposited Zn for different deposition durations. In the pure $ZnBr_2$ electrolyte, the intensity ratio of the $(100)_{Zn}$ and $(002)_{Zn}$ facets decreases from 1.89 to 1.24 (Fig. 2f). Conversely, in the Gd^{3+}–$ZnBr_2$ electrolyte, the intensity ratio of the $(101)_{Zn}$ peak to the $(002)_{Zn}$ peak increases from 1.71 to 2.13, along with the increase in the capacity of deposited Zn, indicating a distinct preferential growth of the $(101)_{Zn}$ facet (Fig. 2g and Table S1†). Furthermore, the X-ray pole figure results also reveal the $(101)_{Zn}$ facet dominates and uniformly distributes the deposited Zn from the Gd^{3+}–$ZnBr_2$ electrolyte (Fig. S7†).

2.2 Preferential adsorption of Gd^{3+} ions in the IHP for a uniform Zn morphology

To explore the preferential growth of the $(101)_{Zn}$ plane, molecular dynamics (MD) simulations are conducted to study the adsorption behaviors of Gd^{3+} ions on different Zn crystal facets. The number of ions, molecules, total atoms, and the size of the simulation box for the modeling system are shown in Table S2.† Specifically, three Zn facet models are studied on $(002)_{Zn}$, $(100)_{Zn}$, and $(101)_{Zn}$ planes in the hexagonal close-packed crystal structure of Zn metal according to the XRD results (Fig. 3a–c and S8†),[35,36] respectively, where the Gd^{3+}–$ZnBr_2$ electrolyte is applied to the planar Zn electrodes with different facets (Fig. S9†).

The numbers of cations adsorbed onto the interfacial IHP of the $(002)_{Zn}$, $(100)_{Zn}$, and $(101)_{Zn}$ crystal facets are shown in Fig. 3d, S10 and Table S3.† Specifically, the numbers of Gd^{3+} ions on the surface of the $(002)_{Zn}$, $(100)_{Zn}$, and $(101)_{Zn}$ crystal

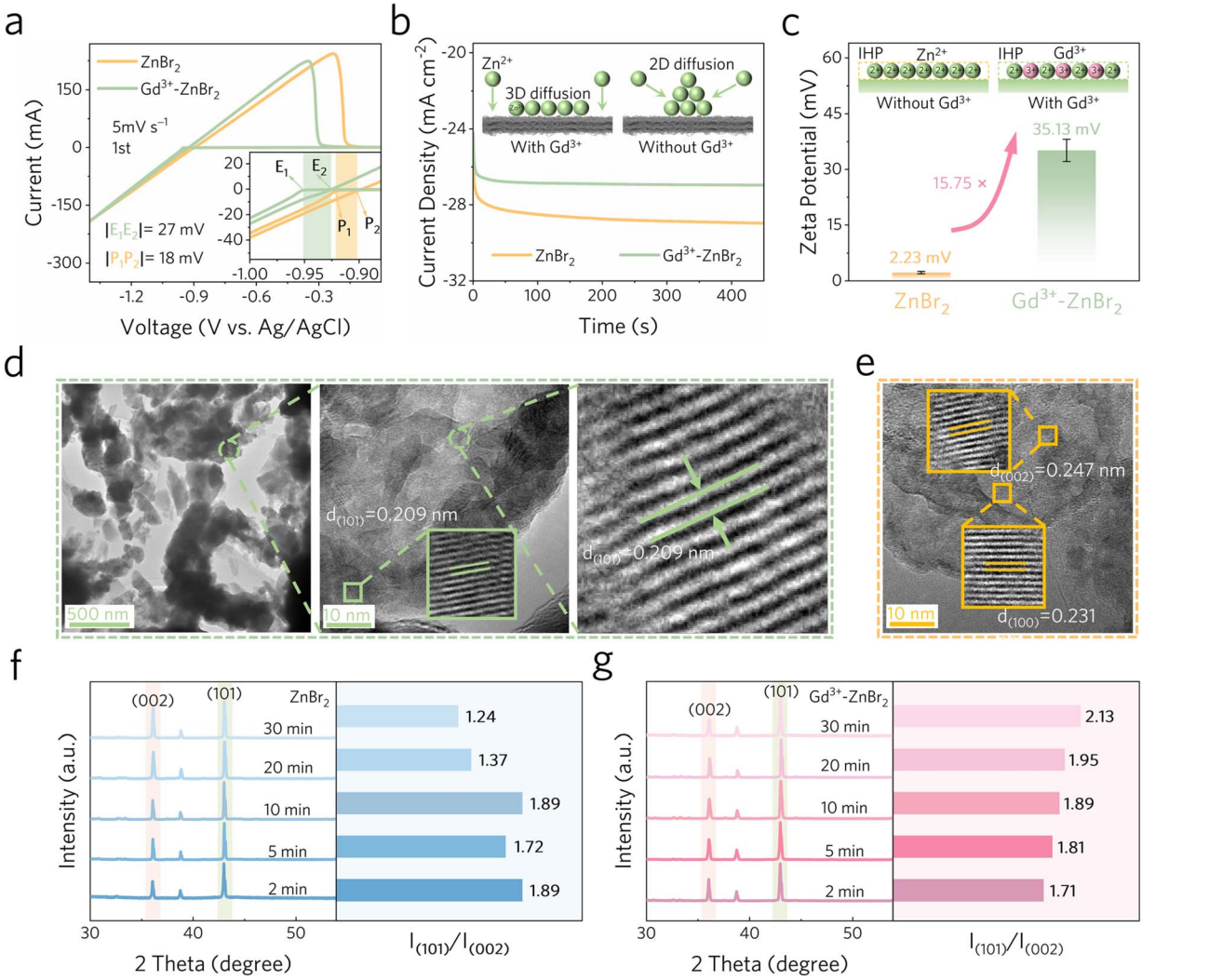

Fig. 2 Electrochemical and Zn facet growth behaviors of the Zn@CF anode. (a) CV profiles in $ZnBr_2$ and Gd^{3+}–$ZnBr_2$ electrolytes with a three-electrode system, and the inset shows the overpolarized potential for Zn nucleation. (b) CA trails for the Zn nucleation process in $ZnBr_2$ and Gd^{3+}–$ZnBr_2$ electrolytes, respectively. (c) Zeta potentials of Zn metal in $ZnBr_2$ and Gd^{3+}–$ZnBr_2$ electrolytes, with the inset illustrating the ion adsorption mechanism at the inner IHP. (d) HRTEM images of the deposited Zn inside the Gd^{3+}–$ZnBr_2$ electrolyte and the (e) $ZnBr_2$ electrolyte, respectively. (f) and (g) XRD of Zn crystal growth behavior on CF at 20 mA cm^{-2} in the $ZnBr_2$ and Gd^{3+}–$ZnBr_2$ electrolytes.

facets are 12, 11, and 7, respectively. On the other hand, the corresponding numbers of Zn^{2+} ions on the $(002)_{Zn}$, $(100)_{Zn}$, and $(101)_{Zn}$ crystal facets are 50, 58, and 69, respectively. Thus, the higher number of Gd^{3+} ions and the lower number of Zn^{2+} ions indicate competitive adsorption between Gd^{3+} and Zn^{2+} ions, leading to the formation of the Gd^{3+}-enriched IHP on the $(002)_{Zn}$ and $(100)_{Zn}$ facets. These competitive adsorption behaviors correlate with the steric hindrance and electrostatic shielding effects. The adsorbed Gd^{3+} ions can repel the subsequent adsorption of Zn^{2+} ions on the surface of $(002)_{Zn}$ and $(100)_{Zn}$ planes, thereby promoting preferential Zn deposition onto the $(101)_{Zn}$ plane. This is further supported by the lower adsorption energy of Gd^{3+} ions on the Zn $(101)_{Zn}$ crystal facet with less electrostatic repulsion, which is lower (−111.62 eV) than those of the $(002)_{Zn}$ facet (−134.28 eV) and the $(100)_{Zn}$ facet (−134.01 eV), as shown in Fig. 3e.

Subsequently, the deposited Zn morphologies for 10, 15, 20, and 30 minutes in different electrolytes are analyzed. As shown in Fig. 3f, the scanning electron microscopy (SEM) images show a gradual increase in the size of Zn clusters with a coarse morphology as the Zn deposition capacity increases. It leads to the formation of more dendritic structures on the carbon felt in the pure $ZnBr_2$ electrolyte. In contrast, the deposited Zn in the Gd^{3+}–$ZnBr_2$ electrolyte exhibits a uniform and dense Zn morphology composed of fine-grained Zn nucleation, which promotes a dendrite-free morphology. The surface morphology evolution of the deposited Zn in two different electrolytes is monitored *in situ*, where the flat Zn foil electrode is employed to facilitate direct observation of Zn deposition morphology (Fig. S11†). As shown in Fig. S12,† the Zn electrode deposited at 20 mA cm^{-2} in the control pure $ZnBr_2$ electrolyte exhibits uneven protrusions after 1.67 mA h cm^{-2} deposition, and these

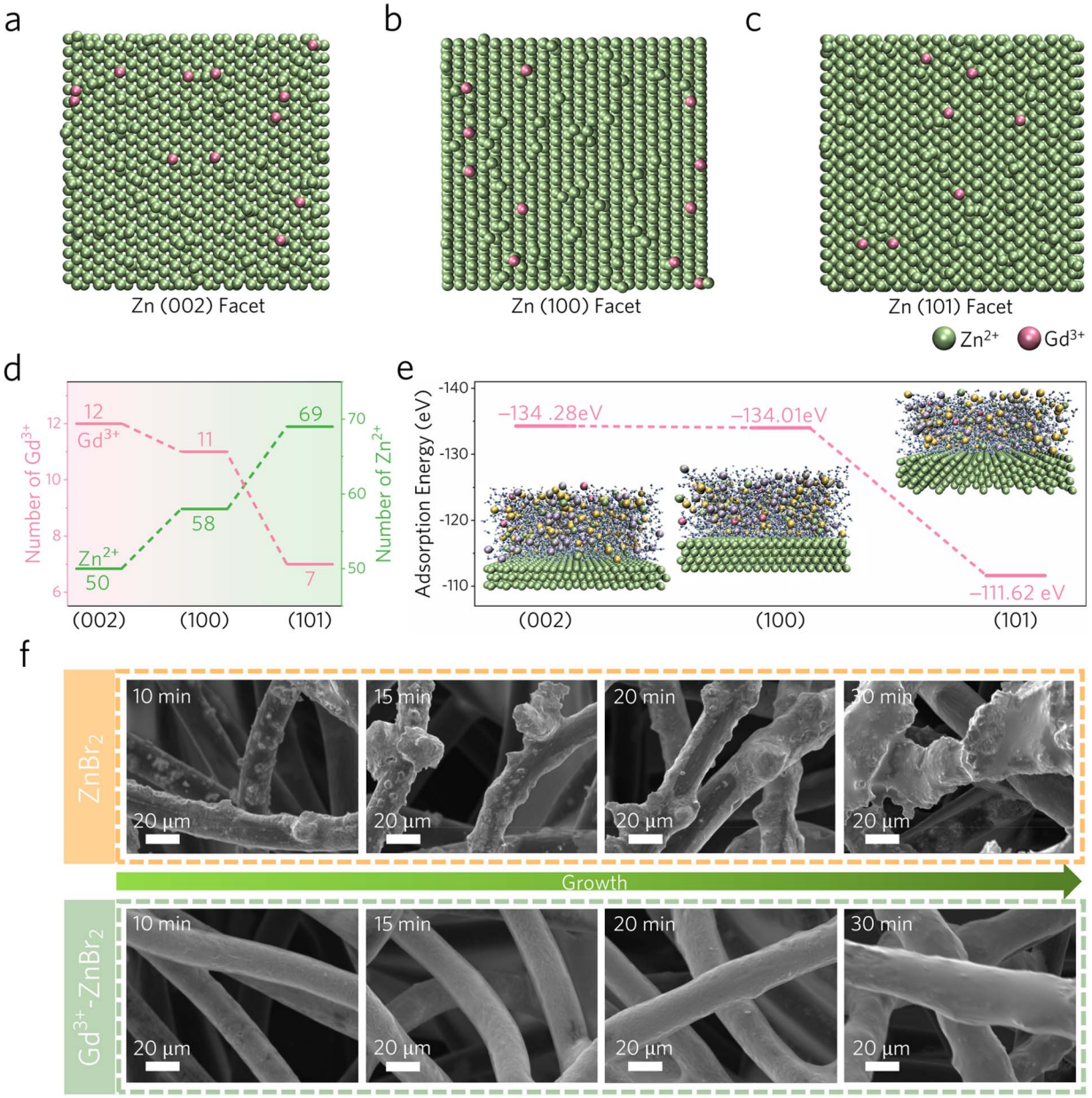

Fig. 3 Gd^{3+}/Zn^{2+} adsorption on different Zn facets and the deposited Zn morphologies. (a–c) Interfacial layering IHP structure configurations of different Zn facets obtained from MD simulations. (d) Analysis of the numbers of different ions in the interfacial layer of the $(002)_{Zn}$, $(100)_{Zn}$, and $(101)_{Zn}$ crystal facets. (e) Adsorption energy of Gd^{3+} ions on different Zn facets. (f) SEM images of Zn crystal growth behavior on CFs after being deposited at 20 mA cm^{-2} in the $ZnBr_2$ and Gd^{3+}–$ZnBr_2$ electrolytes.

protrusions become more pronounced after 5 mA h cm^{-2}, eventually forming mossy-like Zn dendrites. In contrast, the Zn electrode deposited in the Gd^{3+}–$ZnBr_2$ electrolyte maintained a flat and dense surface of Zn deposits. This *in situ* observation of Zn deposition morphology further verifies the improving effect of Gd^{3+} ions in promoting oriented crystal growth.

2.3 Dynamic electrostatic shielding effect of Gd^{3+} ions in IHP

Based on the above results, it is proposed that the Zn electrodeposition behaviors are regulated by the preferential adsorption of Gd^{3+} ions inside the IHP.[23,37] Specifically, cations are adsorbed onto the Zn deposit interface of 3D carbon felt, creating a Gd^{3+}-enriched and positively charged IHP (Fig. 4a and b). It results in the surface potentials shifting from Ψ_0 to Ψ_ξ and ψ'_ξ, respectively, corresponding to the $ZnBr_2$ and the Gd^{3+}–$ZnBr_2$ electrolytes.[38,39] In the Gd^{3+}–$ZnBr_2$ electrolyte, Gd^{3+} ions preferentially adsorb inside the IHP to impart a higher net positive charge to the electrode surface. The Gd^{3+}-enriched IHP enables electrostatic repulsion to prevent Zn^{2+} ion aggregation, minimizes the electrostatic potential gradient, and stabilizes the IHP with a more uniform ion distribution.[40] The stronger electrostatic repulsion prevents Zn^{2+} ion aggregation and dendrite growth. Accordingly, Gd^{3+} ions exhibit higher adsorption

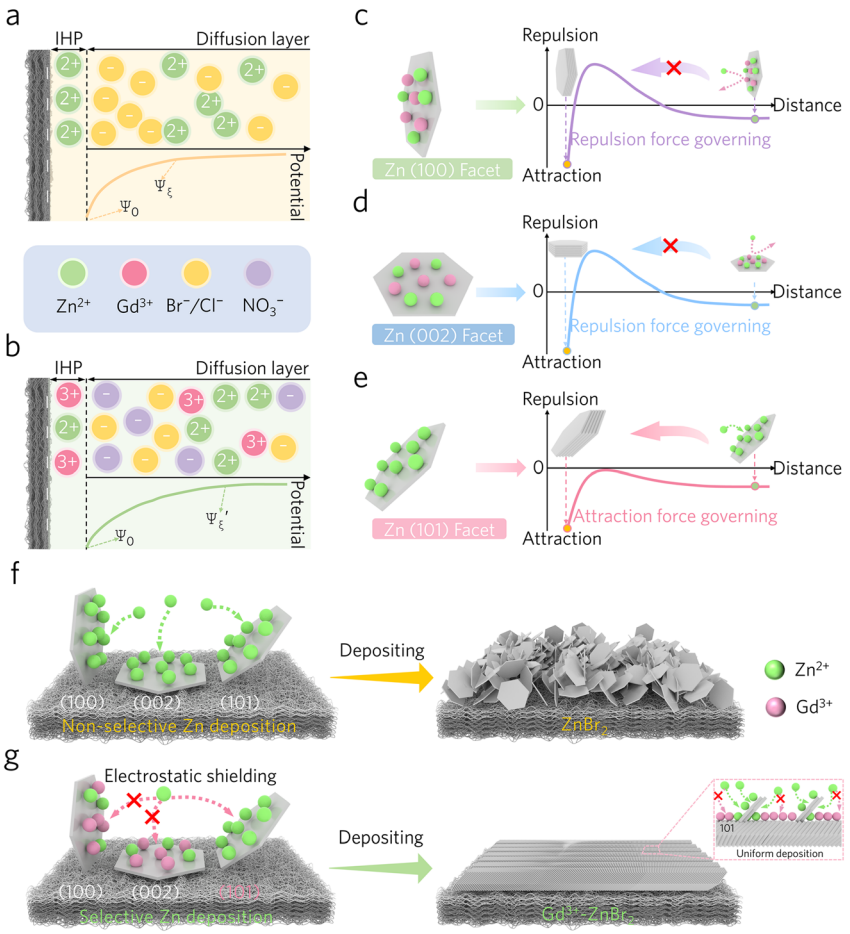

Fig. 4 Schematic of Zn^{2+} deposition behaviors induced by the IHP with the electrostatic shielding effect modulated by preferential Gd^{3+} adsorption. Comparison of interfacial potentials for Zn deposition in (a) $ZnBr_2$ and (b) Gd^{3+}–$ZnBr_2$ electrolytes. (c–e) Growth models of the Zn deposits on different crystal facets in Gd^{3+}–$ZnBr_2$ electrolytes. (f and g) Diagram of the Zn deposition morphology in the $ZnBr_2$ and Gd^{3+}–$ZnBr_2$ electrolytes.

energy, with more Gd^{3+} ions adsorbed on the $(002)_{Zn}$ and $(100)_{Zn}$ crystal facets, forming a dynamic electrostatic shielding layer that retards Zn growth kinetics, as shown in Fig. 4c and d. In contrast, Gd^{3+} ions exhibit lower adsorption energy on the $(101)_{Zn}$ facet, with fewer Gd^{3+} ions adsorbed and less electrostatic shielding for Zn^{2+} ions, leading to preferential deposition on the $(101)_{Zn}$ facet (Fig. 4e). Ultimately, in the $ZnBr_2$ electrolyte, the unstable IHP causes random deposition and dendrite formation (Fig. 4f), whereas, in the Gd^{3+}–$ZnBr_2$ electrolyte, the enhanced IHP stability promotes orderly Zn deposition on the $(101)_{Zn}$ facet (Fig. 4g). The predominance of Zn deposition on the (101) facet creates a uniform electrochemical environment across the electrode surface, ensuring consistent nucleation and growth conditions on all active sites. This uniformity prevents preferential deposition at specific locations, thereby suppressing dendrite formation and enhancing the reversibility of the Zn@CF anode.

2.4 Suppressed HER by the proton shielding effect of the reconstructed IHP

Besides the uncontrolled Zn dendrites, the HER is another undesirable side reaction on the Zn@CF electrode. Linear sweep voltammetry (LSV) is performed in two different electrolytes, showing that the Zn electrode in the Gd^{3+}–$ZnBr_2$ electrolyte exhibits a 10 mV larger HER overpotential compared to that in the pure $ZnBr_2$ electrolyte (Fig. 5a). Furthermore, according to the Tafel results, the corrosion current density in the pure $ZnBr_2$ electrolyte, which is 13.5 mA cm^{-2}[c], is significantly larger compared to that of the Zn electrode in the Gd^{3+}–$ZnBr_2$ electrolyte (8.5 mA cm^{-2}, Fig. 5b). To further assess the HER inhibitory effect, Zn||Zn symmetric flow batteries are assembled based on the two electrolytes and cycled at 50 mA cm^{-2} (5 mA h cm^{-2}) for 50 cycles. After cycling, the Zn anodes are analyzed using X-ray diffraction (XRD), showing that the Zn@CF electrode cycled in the pure $ZnBr_2$ electrolyte exhibits a large amount of $Zn_5(OH)_8Br_2{\cdot}H_2O$ byproducts (Fig. 5c),[16] which originated from the HER as shown in the following formulation:

$$3Zn(OH_2)_6^{2+} + 2Zn^{2+} + 2Br^- + (2x-8)H^+ + 2xe^- \rightarrow Zn_5(OH)_8Br_2{\cdot}H_2O + 9H_2O + xH_2\uparrow$$

In contrast, only metallic Zn is observed on the anode, with no by-products found in the battery cycled in the Gd^{3+}–$ZnBr_2$

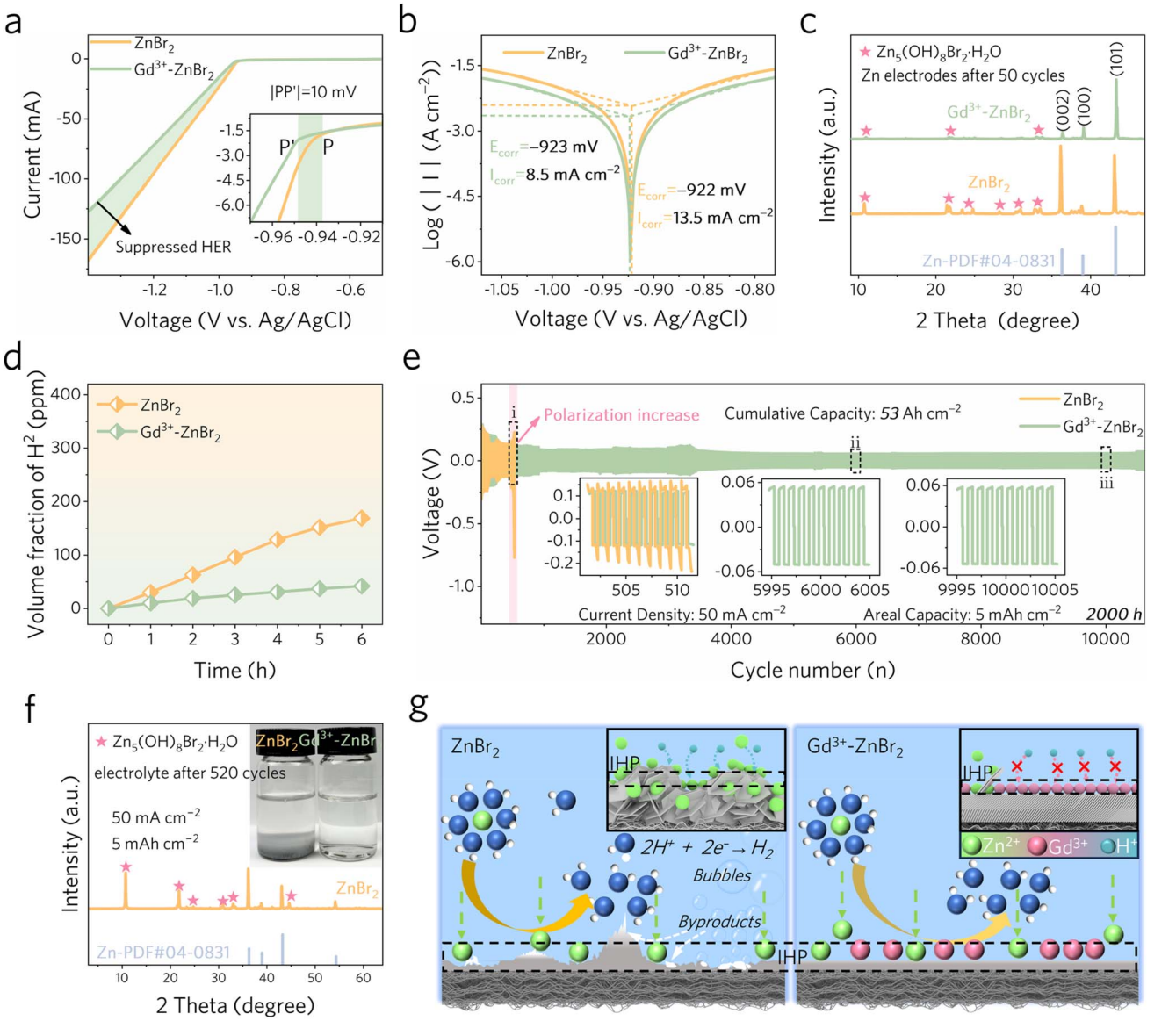

Fig. 5 Analysis of Zn@CF anode reversibility. (a) LSV profiles of Zn electrodes in the $ZnBr_2$ and Gd^{3+}–$ZnBr_2$ electrolytes. (b) Tafel curves in the $ZnBr_2$ and Gd^{3+}–$ZnBr_2$ electrolytes. (c) XRD patterns of deposited Zn after 50 cycles of the Zn||Zn symmetric flow batteries at a current density of 50 mA cm^{-2} and 5 mA h cm^{-2}, demonstrating reduced byproducts in the Gd^{3+}–$ZnBr_2$ electrolyte. (d) The volume variations of H_2 during cycling. (e) Voltage profiles of Zn||Zn flow batteries utilizing $ZnBr_2$ and Gd^{3+}–$ZnBr_2$ electrolytes at 50 mA cm^{-2} and 5 mA h cm^{-2}, and the insets show the amplified voltage profile in different cycles. (f) XRD patterns of precipitates in $ZnBr_2$ electrolyte after 520 cycles at 50 mA cm^{-2} and 5 mA h cm^{-2}, and the inset shows the containers of $ZnBr_2$ and Gd^{3+}–$ZnBr_2$ electrolytes after 520 cycles, respectively. (g) Diagram of the Gd^{3+}-enriched IHP suppressing undesirable parasitic reactions, and the insets show the influence of the IHP on protons.

electrolyte. These results reveal the stabilizing effect of Gd^{3+} ions in inhibiting HER side reactions for enhanced reversibility of Zn@CF electrodes.

The volume of hydrogen produced at the Zn@CF anode is *in situ* characterized in the flow battery configuration based on different electrolytes. The variation in H_2 evolution flux throughout the battery cycling process is shown in Fig. 5d.[41] At a current density of 40 mA cm^{-2} with a deposition capacity of 5 mA h cm^{-2} per cycle, the amount of H_2 evolution in the $ZnBr_2$ electrolyte reached 30 ppm after 1 hour (4 cycles). After 6 hours of operation (24 cycles), the H_2 content in the $ZnBr_2$ electrolyte rises to 169 ppm, which is four times higher than the 42 ppm in the Gd^{3+}–$ZnBr_2$ electrolyte, where the HER is effectively suppressed. On the other hand, it can also be confirmed by *in situ* measurements of the pH variations in the electrolyte on the Zn@CF anode side of the flow battery. Throughout the 6-hour test, the pH of the Gd^{3+}–$ZnBr_2$ electrolyte remains relatively stable with a smaller variation (from 4.20 to 4.56) compared to the pure $ZnBr_2$ electrolyte (from 4.20 to 4.90), which can be attributed to the less H_2 evolution and the consequent OH^- produced (Fig. S13†).[42–44] By measuring the variations in H_2

evolution flux and pH values, the Gd^{3+}–$ZnBr_2$ electrolyte is shown to inhibit irreversible HER at the Zn@CF anode.

To further assess the impact of the Gd^{3+}-enriched IHP on the performance of Zn-based flow batteries, Zn‖Zn symmetric flow batteries with different electrolytes are characterized at various current densities ranging from 20 to 100 mA cm^{-2} (Fig. S14a†). The voltage hysteresis values of the Gd^{3+}–$ZnBr_2$ electrolyte range from 58 to 260 mV, higher than those of the pure $ZnBr_2$ electrolyte, which range from 52 to 240 mV. As shown in Fig. S14b,† the exchange current density (i_0) of the Gd^{3+}–$ZnBr_2$ electrolyte is relatively lower at 21.22 mA cm^{-2} than that of the pure $ZnBr_2$ electrolyte of 22.37 mA cm^{-2}. This is related to the relatively slow kinetics of Zn electrodeposition, which promotes preferential growth on the $(101)_{Zn}$ plane. The Zn‖Zn symmetric flow batteries are tested to evaluate the cycling stability of the Zn@CF anode in two different electrolytes. At a high current of 100 mA cm^{-2} and an areal capacity of 10 mA h cm^{-2}, the Zn‖Zn symmetric flow battery using the Gd^{3+}–$ZnBr_2$ electrolyte exhibits markedly improved cycling stability. It lasts for over 4900 cycles, with a cumulative areal capacity of 49 A h cm^{-2}. This performance is approximately 15.3 times longer than that of the battery using the pure $ZnBr_2$ electrolyte, which only lasts for 320 cycles (Fig. S15†). Moreover, at a smaller areal capacity of 5 mA h cm^{-2} at 50 mA cm^{-2}, the Zn‖Zn symmetric flow battery with the Gd^{3+}–$ZnBr_2$ electrolyte maintains stable operation over 10 000 cycles and 2000 hours (Fig. 5e). This leads to a cumulative areal capacity of 53 A h cm^{-2}, approximately 20 times longer than the battery with the pure $ZnBr_2$ electrolyte, which lasts only 520 cycles. The increased polarization in the control Zn‖Zn cell results from uneven Zn deposition and accumulation of insulating byproducts, which increase interfacial resistance and hinder ion transport. This leads to deteriorated electrode kinetics and reduced reversibility, ultimately causing cell failure.

It should be noted that there is a chance for "soft shorts" (SS) in the symmetric batteries to overestimate the cycling stability,[45] which refers to the small localized electrical connection between two electrodes that enable the coexistence of direct electron transfer and interfacial reaction.[46,47] To verify it, EIS is performed during the cycling of the Zn‖Zn symmetric flow batteries at a high current density of 100 mA cm^{-2}. Due to differences in interfacial reaction kinetics and diffusion limitations, the voltage curve of a standard symmetric battery typically exhibits a slope (Fig. S16a†). Moreover, as illustrated in Fig. S16b,† the impedance R_{ct} at different cycle numbers (1st/25th/50th/250th) was tested. There are no sudden drops of R_{ct}, which indicates that there are no soft shorts during the long-term cycling by utilizing the Gd^{3+}–$ZnBr_2$ electrolyte.[45]

To further elucidate the role of the Gd^{3+} ions in improving the cycling stability of flow batteries, the electrolytes of the batteries after cycling are investigated. As shown in the inset of Fig. 5f, the flow battery using the pure $ZnBr_2$ electrolyte contained many gray-color precipitates in the control electrolyte tank after 520 cycles (when the control battery fails) at 50 mA cm^{-2} and 5 mA h cm^{-2}. These precipitates are likely byproducts and dead Zn generated during battery cycling, which is collected and identified as $Zn_5(OH)_8Br_2 \cdot H_2O$ and Zn metal according to the XRD results. In contrast, the Gd^{3+}–$ZnBr_2$ electrolyte remains clean with no precipitates (Fig. 5f). Similar findings can be seen after 320 cycles at a larger current of 100 mA cm^{-2} and a larger areal capacity of 10 mA h cm^{-2} (when the control battery fails in the pure $ZnBr_2$ electrolyte) (Fig. S17†). These results demonstrate that enhancing the stability of the IHP effectively improves the reversibility of the Zn@CF anode in flow batteries.

The inhibition of Zn dendrite formation and the HER by applying a stable IHP is illustrated in Fig. 5g. Specifically, in the pure $ZnBr_2$ electrolyte, the unstable IHP leads to concentration polarization and an uneven electric field, causing Zn^{2+} ions to laterally diffuse across the IHP and deposit at energetically favorable sites. Therefore, it results in Zn dendrite formation and exaggerates the HER as the irreversible Zn@CF anode. In contrast, the preferential adsorption of Gd^{3+} ions restructures and stabilizes the Gd^{3+}-enriched IHP with a dynamic electrostatic shielding layer, which prevents the direct contact between the Zn@CF electrode and protons in the electrolyte, thereby suppressing the HER and the by-product formation.

2.5 Performance of ZBFBs based on the Gd^{3+}-enriched IHP

ZBFBs based on Gd^{3+}–$ZnBr_2$ and the $ZnBr_2$ negolytes are assembled, respectively (Fig. 6a), which are cycled at different current densities ranging from 20 to 100 mA cm^{-2}. The rate performance and the corresponding GCD profiles in Fig. 6b, c, and S18† confirm that Gd^{3+}–$ZnBr_2$ as the negolyte is superior to the pure $ZnBr_2$ negolyte. Specifically, flow batteries assembled with the Gd^{3+}–$ZnBr_2$ negolyte exhibited higher CE and EE due to the significantly enhanced electrode/negolyte interfacial electrochemical stability, as proven above.

The ZBFBs assembled with the pure $ZnBr_2$ negolyte show a sharp decline in CE after 150 hours of cycling at a current density of 20 mA cm^{-2} and an areal capacity of 10 mA h cm^{-2}, as shown in Fig. 6d. In sharp contrast, the ZBFB based on the Gd^{3+}–$ZnBr_2$ negolyte operates stably up to 3300 hours, and it achieves a cumulative areal capacity of over 33 A h cm^{-2}, which represents a 22-fold increase in cycling lifetime compared to the control pure $ZnBr_2$-based ZBFB. Cumulative areal capacity serves as a key parameter for quantifying the total zinc deposition and stripping during cycling.[8,48] A higher cumulative areal capacity correlates with improved cycling stability and reversibility of the zinc anode, which are critical for maintaining high energy and consistent energy storage. Moreover, the ZBFB operates continuously for 2000 cycles based on the Gd^{3+}–$ZnBr_2$ negolyte at a higher current density of 40 mA cm^{-2} and an areal capacity of 5 mA h cm^{-2}, achieving a cumulative areal capacity of 10 A h cm^{-2}. As for the flow battery with pure $ZnBr_2$ negolyte, only 150 cycles are realized (Fig. 6e). The inferior performance of the battery with pure $ZnBr_2$ negolyte could be attributed to the continuous accumulation of Zn dendrites, irreversible HER, and byproducts on the anode side, causing short circuits in ZBFBs. Additionally, the selected GCD profiles of ZBFBs, corresponding to Fig. 6d and e, are presented in Fig. S19.† The profiles show that batteries assembled with pure $ZnBr_2$ negolyte begin to fluctuate, with a significant decline in CE around 150 cycles. The corresponding time–voltage curves are exhibited in

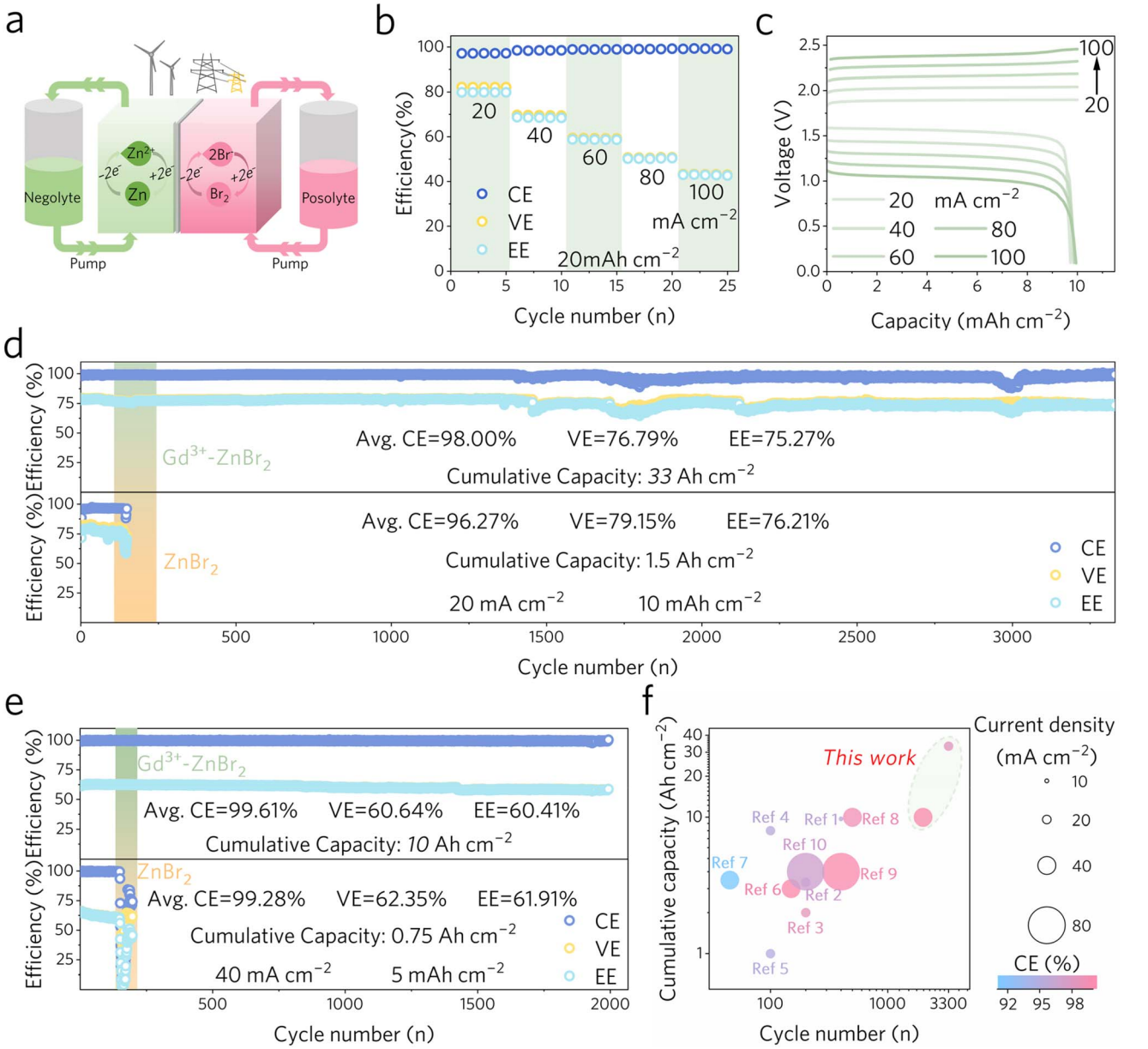

Fig. 6 Energy efficiencies assessment of ZBFBs. (a) Schematic of a highly reversible ZBFB. (b) Rate performance and (c) the corresponding charge–discharge curves at different current densities. (d) The cycling performance of the ZBFB at a current density of 20 mA cm^{-2} with an areal capacity of 10 mA h cm^{-2}, and (e) at a current density of 40 mA cm^{-2} with an areal capacity of 5 mA h cm^{-2}. (f) Comparison of current density, coulombic efficiency, cycle number, and cumulative capacity between our work and other reported cutting-edge studies on the reversibility of Zn@CF anodes in ZBFBs, and the details are listed in Table S4.†

Fig. S20† and the obvious voltage fluctuations can be observed at the point of battery failure (inset of Fig. S20†).

Lastly, the cumulative areal capacity and cycling stability are superior those of previously reported ZBFBs (Fig. 6f; the comparison details are shown in Table S4†). Specifically, the cumulative capacity achieved is 33 A h cm^{-2} at a current density of 20 mA cm^{-2} by applying the Gd^{3+}–$ZnBr_2$ negolyte, which exceeds other cumulative capacities compared to previously reported studies on Zn@CF anode reversibility in ZBFBs. This highlights the effectiveness of stabilizing the IHP in improving battery performance.

3 Conclusion

In summary, a Gd^{3+}-enriched IHP is reconstructed to significantly improve the reversibility of the Zn anode and cycling performance in ZBFBs, which acts as an electrostatic shielding layer to ensure uniform ion concentration and electric field distribution. The inert and dynamic nature of the reconstructed IHP makes it highly suitable for three-dimensional electrodes in flow batteries. It mitigates concentration polarization and tip effects, while simultaneously promoting preferential growth on the Zn (101) crystal facet and suppressing the HER. As a result,

the ZBFB achieves ultra-long cycling stability, with 3300 hours of charge–discharge cycling and a cumulative capacity of 33 A h cm^{-2} at 20 mA cm^{-2}, representing a 22-fold increase in cycling lifetime compared to the control $ZnBr_2$ negolyte. This study highlights rare-earth Gd^{3+} ions as a highly effective additive for enhancing IHP stability and Zn anode reversibility, providing valuable insights for developing high-performance Zn-based flow batteries.

Data availability

The authors declare that all the data supporting the findings of this study are available within the article and its ESI† or from the corresponding author upon reasonable request.

Conflicts of interest

The authors declare no conflict of interest.

Acknowledgements

This research was supported by the Shenzhen Science and Technology Program JCYJ20230807142508016, Guangdong Basic and Applied Basic Research Foundation 2024A1515010915, the Shenzhen Science and Technology Program (Grant No. RCBS20231211090650089), the National Natural Science Foundation of China (22409138 and 52471154), the Excellent Youth Fund of Anhui Province (2108085Y17), the Major Project of Anhui Provincial University Science Research Program (2024AH040013), and the Opening Foundation Program of Shanxi Provincial Key Laboratory for High Performance Battery Materials and Devices (2023HPBMD01001).

References

1 C. Wang, W. Lu, Q. Lai, P. Xu, H. Zhang and X. Li, *Adv. Mater.*, 2019, **31**, 1904690.
2 C. Wang, Q. Lai, P. Xu, D. Zheng, X. Li and H. Zhang, *Adv. Mater.*, 2017, **29**, 1605815.
3 J.-H. Lee, Y. Byun, G. H. Jeong, C. Choi, J. Kwen, R. Kim, I. H. Kim, S. O. Kim and H.-T. Kim, *Adv. Mater.*, 2019, **31**, 1970366.
4 F. Wang, O. Borodin, T. Gao, X. Fan, W. Sun, F. Han, A. Faraone, J. A. Dura, K. Xu and C. Wang, *Nat. Mater.*, 2018, **17**, 543–549.
5 J. Noack, N. Roznyatovskaya, T. Herr and P. Fischer, *Angew. Chem., Int. Ed.*, 2015, **54**, 9776–9809.
6 Z. Yuan, Y. Yin, C. Xie, H. Zhang, Y. Yao and X. Li, *Adv. Mater.*, 2019, **31**, 1970356.
7 H. Jia, Z. Wang, B. Tawiah, Y. Wang, C.-Y. Chan, B. Fei and F. Pan, *Nano Energy*, 2020, **70**, 104523.
8 Y. Yao, J. Lei, Y. Shi, F. Ai and Y.-C. Lu, *Nat. Energy*, 2021, **6**, 582–588.
9 S. Wang, Z. Wang, Y. Yin, T. Li, N. Chang, F. Fan, H. Zhang and X. Li, *Energy Environ. Sci.*, 2021, **14**, 4077–4084.
10 D. Lin and Y. Li, *Adv. Mater.*, 2022, **34**, 2108856.
11 W. Xie, K. Zhu, H. Yang and W. Yang, *Adv. Mater.*, 2024, **36**, 2306154.
12 L. Jiang, D. Li, X. Xie, D. Ji, L. Li, L. Li, Z. He, B. Lu, S. Liang and J. Zhou, *Energy Storage Mater.*, 2023, **62**, 102932.
13 S. jiao, J. Fu, Q. Yin, H. Yao and H. Hu, *Energy Storage Mater.*, 2023, **59**, 102774.
14 K. Fu, T. Liu, M. Xie, Y. Wu, Z. Li, Y. Xin, Y. Liao, C. Liu, H. Huang, D. Ma, F. Zeng and X. Liang, *Adv. Funct. Mater.*, 2024, **34**, 2407895.
15 T. Yan, M. Tao, J. Liang, G. Zheng, B. Wu, L. Du, Z. Cui and H. Song, *Energy Storage Mater.*, 2024, **65**, 103190.
16 L. Qian, W. Yao, R. Yao, Y. Sui, H. Zhu, F. Wang, J. Zhao, C. Zhi and C. Yang, *Adv. Funct. Mater.*, 2021, **31**, 2105736.
17 T. Wu, C. Hu, Q. Zhang, Z. Yang, G. Jin, Y. Li, Y. Tang, H. Li and H. Wang, *Adv. Funct. Mater.*, 2024, **34**, 2315716.
18 J. Luo, L. Xu, Y. Yang, S. Huang, Y. Zhou, Y. Shao, T. Wang, J. Tian, S. Guo, J. Zhao, X. Zhao, T. Cheng, Y. Shao and J. Zhang, *Nat. Commun.*, 2024, **15**, 6471.
19 J. Luo, L. Xu, Y. Zhou, T. Yan, Y. Shao, D. Yang, L. Zhang, Z. Xia, T. Wang, L. Zhang, T. Cheng and Y. Shao, *Angew. Chem., Int. Ed.*, 2023, **135**, e202302302.
20 L. Liu, X. Wang, Z. Hu, X. Wang, Q. Zheng, C. Han, J. Xu, X. Xu, H.-K. Liu, S.-X. Dou and W. Li, *Angew. Chem., Int. Ed.*, 2024, **63**, e202405209.
21 Y. Wang, J. Lv, L. Hong, J. Zhang, C. Chen, A. Xu, M. Huang, X. Ren, J. Bai, H. Wang and X. Liu, *Angew. Chem., Int. Ed.*, 2025, **64**, e202414757.
22 G. Gao, X. Huo, B. Li, J. Bi, Z. Zhou, Z. Du, W. Ai and W. Huang, *Energy Environ. Sci.*, 2024, **17**, 7850–7859.
23 Z.-F. Wang, C. Tang, Q. Sun, Y.-L. Han, Z.-J. Wang, L. Xie, S.-C. Zhang, F.-Y. Su and C.-M. Chen, *J. Energy Chem.*, 2023, **80**, 120–127.
24 Y. Chen, Z. Deng, Y. Sun, Y. Li, H. Zhang, G. Li, H. Zeng and X. Wang, *Nano-Micro Lett.*, 2024, **16**, 96.
25 Y. Yang, H. Hua, Z. Lv, M. Zhang, C. Liu, Z. Wen, H. Xie, W. He, J. Zhao and C. C. Li, *Adv. Funct. Mater.*, 2023, **33**, 2212446.
26 T. P. Moffat, D. Wheeler and D. Josell, *J. Electrochem. Soc.*, 2004, **151**, C262.
27 A. Bayaguud, X. Luo, Y. Fu and C. Zhu, *ACS Energy Lett.*, 2020, **5**, 3012–3020.
28 N. Ullah, M. Imran, K. Liang, C.-Z. Yuan, A. Zeb, N. Jiang, U. Y. Qazi, S. Sahar and A.-W. Xu, *Nanoscale*, 2017, **9**, 13800–13807.
29 Y. Ding, X. Zhang, T. Wang, B. Lu, Z. Zeng, Y. Tang, J. Zhou and S. Liang, *Energy Storage Mater.*, 2023, **62**, 102949.
30 J. Cao, J. Wu, H. Wu, Y. Jin, D. Luo, X. Yang, L. Zhang, D. Zhang, J. Qin and J. Lu, *Adv. Funct. Mater.*, 2024, **34**, 2401537.
31 Z. Hu, F. Zhang, Y. Zhao, H. Wang, Y. Huang, F. Wu, R. Chen and L. Li, *Adv. Mater.*, 2022, **34**, 2203104.
32 C. Wang, X. Zeng, J. Qu, J. M. Cairney, Q. Meng, P. J. Cullen and Z. Pei, *Matter*, 2023, **6**, 3993–4012.
33 C. Yan, H.-R. Li, X. Chen, X.-Q. Zhang, X.-B. Cheng, R. Xu, J.-Q. Huang and Q. Zhang, *J. Am. Chem. Soc.*, 2019, **141**, 9422–9429.

34 K. Tang, J. Fu, M. Wu, T. Hua, J. Liu, L. Song and H. Hu, *Small Methods*, 2022, **6**, 2101276.
35 F. C. Frank, J. H. Van Der Merwe and N. F. Mott, *Proc. R. Soc. Lond. A Math. Phys. Sci.*, 1997, **198**, 216–225.
36 Q. Liu, X. Liu, Y. Liu, M. Huang, W. Wang, Y. Cheng, H. Zhang and L. Xu, *ACS Nano*, 2024, **18**, 4932–4943.
37 S. Li, J. Zhao, X. Xu, J. Shen, K. Zhang, X. Chen, K. Wang, X. Jiao, Z. Wang, D. Xu, Q. Zhang, Y. Liu and Y. Bai, *Mater. Today*, 2024, **80**, 50–60.
38 X. Guo, J. Lu, M. Wang, A. Chen, H. Hong, Q. Li, J. Zhu, Y. Wang, S. Yang, Z. Huang, Y. Wang, Z. Pei and C. Zhi, *Chem*, 2024, **10**, 3607–3621.
39 G. Yang, Q. Zhang, Z. Liu, J. Song, Z. Yin, Y. Zhao, S. Jiang, J. Han, X. Li, H. Yang, S. He and Z. Pei, *Adv. Energy Mater.*, 2025, 2501358.
40 Z. He, L. Pan, Z. Peng, Z. Liu, Z. Zhang, B. Li, Z. Zhang, X. Wu, N. Zhao, L. Dai, Z. Zhuang, L. Wang and Q. Zhang, *Adv. Energy Mater.*, 2025, **15**, 2403958.
41 X. Bai, Y. Nan, K. Yang, B. Deng, J. Shao, W. Hu and X. Pu, *Adv. Funct. Mater.*, 2023, **33**, 2307595.
42 Z. Liu, Z. Guo, L. Fan, C. Zhao, A. Chen, M. Wang, M. Li, X. Lu, J. Zhang, Y. Zhang and N. Zhang, *Adv. Mater.*, 2024, **36**, 2305988.
43 C. Lin, X. Yang, P. Xiong, H. Lin, L. He, Q. Yao, M. Wei, Q. Qian, Q. Chen and L. Zeng, *Adv. Sci.*, 2022, **9**, 2201433.
44 W. Zhang, Y. Dai, R. Chen, Z. Xu, J. Li, W. Zong, H. Li, Z. Li, Z. Zhang, J. Zhu, F. Guo, X. Gao, Z. Du, J. Chen, T. Wang, G. He and I. P. Parkin, *Angew. Chem., Int. Ed.*, 2023, **62**, e202212695.
45 Q. Li, A. Chen, D. Wang, Z. Pei and C. Zhi, *Joule*, 2022, **6**, 273–279.
46 M. Sugiyama, C. Wilson, D. Wiedenhofer, B. Boza-Kiss, T. Cao, J. S. Chatterjee, S. Chatterjee, T. Hara, A. Hayashi, Y. Ju, V. Krey, M. F. Godoy León, L. Martinez, E. Masanet, A. Mastrucci, J. Min, L. Niamir, S. Pelz, J. Roy, Y. Saheb, R. Schaeffer, D. Ürge-Vorsatz, B. van Ruijven, Y. Shimoda, E. Verdolini, F. Wiese, Y. Yamaguchi, C. Zell-Ziegler and C. Zimm, *Joule*, 2024, **8**, 1–6.
47 C. Wang, T. Deng, X. Fan, M. Zheng, R. Yu, Q. Lu, H. Duan, H. Huang, C. Wang and X. Sun, *Joule*, 2022, **6**, 1770–1781.
48 L. Ma, M. A. Schroeder, O. Borodin, T. P. Pollard, M. S. Ding, C. Wang and K. Xu, *Nat. Energy*, 2020, **5**, 743–749.